Evaluation of Interpolation Methods for Surface-based Motion Compensated Tomographic Reconstruction for Cardiac Angiographic C-arm Data

Kerstin Müller,* Chris Schwemmer, and Joachim Hornegger
Pattern Recognition Lab, Department of Computer Science,
Erlangen Graduate School in Advanced Optical Technologies (SAOT),
Friedrich-Alexander-Universität Erlangen-Nürnberg, Erlangen 91058, Germany

Yefeng Zheng and Yang Wang
Imaging and Computer Vision, Siemens Corporate Research, Princeton, New Jersey 08540

Günter Lauritsch, Christopher Rohkohl, and Andreas K. Maier
Siemens AG, Healthcare Sector, Forchheim 91301, Germany

Carl Schultz
Thoraxcenter, Erasmus MC, Rotterdam 3000, The Netherlands

Rebecca Fahrig
Department of Radiology, Stanford University, Stanford, California 94305
(Dated: March 1, 2013)

Purpose: For interventional cardiac procedures, anatomical and functional information about the cardiac chambers is of major interest. With the technology of angiographic C-arm systems it is possible to reconstruct intraprocedural three-dimensional 3D images from 2D rotational angiographic projection data (C-arm CT). However, 3D reconstruction of a dynamic object is a fundamental problem in C-arm CT reconstruction. The 2D projections are acquired over a scan time of several seconds, thus the projection data show different states of the heart. A standard FDK reconstruction algorithm would use all acquired data for a filtered backprojection and result in a motion-blurred image. In this approach, a motion compensated reconstruction algorithm requiring knowledge of the 3D heart motion is used. The motion is estimated from a previously presented 3D dynamic surface model. This dynamic surface model results in a sparse motion vector field (MVF) defined at control points. In order to perform a motion compensated reconstruction, a dense motion vector field is required. The dense MVF is generated by interpolation of the sparse MVF. Therefore, the influence of different motion interpolation methods on the reconstructed image quality is evaluated.
Methods: Four different interpolation methods, thin-plate splines (TPS), Shepard's method, a smoothed weighting function, and a simple averaging, were evaluated. The reconstruction quality was measured on phantom data, a porcine model as well as on in vivo clinical data sets. As a quality index, the 2D overlap of the forward projected motion compensated reconstructed ventricle and the segmented 2D ventricle blood pool was quantitatively measured with the Dice similarity coefficient and the mean deviation between extracted ventricle contours. For the phantom data set the normalized root mean square error (nRMSE) and the universal quality index (UQI) were also evaluated in 3D image space.
Results: The quantitative evaluation of all experiments showed that TPS interpolation provided the best results. The quantitative results in the phantom experiments showed comparable nRMSE of $\approx 0.047 \pm 0.004$ for the TPS and Shepard's method. Only slightly inferior results for the smoothed weighting function and the linear approach were achieved. The UQI resulted in a value of $\approx 99\%$ for all four interpolation methods. On clinical human data sets the best results were clearly obtained with the TPS interpolation. The mean contour deviation between the TPS reconstruction and the standard FDK reconstruction improved in the three human cases by 1.52 mm, 1.34 mm and 1.55 mm. The Dice coefficient showed less sensitivity with respect to variations in the ventricle boundary.
Conclusions: In this work, the influence of different motion interpolation methods on left ventricle motion compensated tomographic reconstructions was investigated. The best quantitative reconstruction results of a phantom, a porcine and human clinical data sets were achieved with the TPS approach. In general, the framework of motion estimation using a surface model and motion interpolation to a dense MVF provides the ability for tomographic reconstruction using a motion compensation technique.

Keywords: cardiac motion, motion compensated reconstruction, interpolation methods, C-arm CT

* kerstin.mueller@cs.fau.de; http://www5.cs.fau.de/~mueller

I. INTRODUCTION

A. Purpose of this Work

In interventional procedures, there is increasing interest in three-dimensional imaging of dynamic cardiac shapes, e.g. the left ventricle (LV), for quantitative evaluation of cardiac functions such as ejection fraction measurements and wall motion analysis. An angiographic C-arm CT system is capable of multiple 2D projections while rotating around the patient. With this data a 3D reconstruction of the imaged region is possible. Due to the long acquisition time (a few seconds) of the C-arm, imaging of dynamic structures presents a challenge. The motion of the heart ventricle needs to be taken into account in the reconstruction process. A standard cone-beam reconstruction (FDK) algorithm [1] would use all acquired projections for reconstruction. Consequently, different heart phases cannot be distinguished. The result would be a motion blurred reconstruction of the heart ventricle. A motion compensated tomographic reconstruction for the heart ventricle could overcome the limitations of the FDK approach. In order to compensate for the motion [2], the dynamics of the heart need to be estimated. In this paper, the motion is estimated via a dynamic surface model providing a sparse motion vector field (MVF) [3]. This sparse MVF needs to be interpolated to a dense MVF. Different interpolation methods for this motion compensated tomographic reconstruction technique were investigated. We evaluated a thin-plate spline (TPS) interpolation [4, 5], Shepard's method [6], a simple averaging, and a method using a smoothed weighting function. The interpolation methods were evaluated by comparing the image results of the motion compensated tomographic reconstructions with the gold standard of the original segmented projection data. Additionally, in a numerical phantom experiment the normalized root mean square error (nRMSE) and universal quality index (UQI) were evaluated.

B. State-of-the-Art

Current analysis of heart ventricles is based on observations and measurements directly on the acquired 2D projections [7]. As a first step in evaluation of the ventricular motion in 3D, different approaches for recovering the ventricular shape from angiographic data using biplanar angiographic systems have been described by the group of Medina et al. [8, 9]. Ventricular shape reconstruction from multi-view X-ray projections has been presented by Moriyama et al. [10, 11]. However, with both methods, only a surface model is extracted, providing no morphological or structural information of the ventricle, such as papillary muscles. Cardiologists could benefit from the visualization of the morphological endocardium structure visible in a tomographic reconstruction.

Other approaches use 2D projection data from a whole short-scan. In order to improve temporal resolution, an electrocardiogram (ECG) signal is recorded synchronous with the acquisition. The reconstruction is then performed only with the subset of those projections that lie inside a certain ECG window centered at the favored heart phase [12]. This retrospectively ECG-gated approach works well for sparse and high-contrast structures, e.g. coronaries [13–16]. However, for the heart chambers, an insufficient number of projections are acquired in a single scan. As an example, for a 5 s acquisition time and 60 bpm, only five intervals contribute to one heart phase. As a consequence, multiple sweeps of the C-arm have to be performed in order to acquire enough projections to reconstruct each heart phase with a satisfactory image quality [17, 18]. However, the longer imaging time results in a higher contrast burden and radiation dose for the patient. For sick patients undergoing a cardiac procedure, it might not be possible to hold their breath for several seconds (more than 20 s).

In recent years, approaches using undersampled projection data such as compressed sensing (CS) algorithms have been developed [19]. A number of algorithms minimize an objective function related to the total variation (TV) [20]. In one approach called prior image constrained compressed sensing (PICCS), a-priori information of the same object is incorporated into the reconstruction [21–23]. The PICCS algorithm was recently applied to interventional angiographic C-arm data [24, 25]. It was necessary to use a slower rotation of approximately 14 s to enable a PICCS reconstruction. Chen et al. found that a minimum of at least 14 projections are needed for each heart phase to achieve a good reconstruction result [24].

In this paper, a motion compensated tomographic reconstruction is performed with projection data acquired in one single C-arm rotation (5 s – 8 s). As a first step, a dynamic surface model of the LV is generated [3]. The LV surface model is reconstructed from a set of ECG-gated 2D X-ray projections such that the forward projection of the reconstructed LV model matches the 2D blood pool segmentation of the ventricle. In the second step, a motion compensated tomographic reconstruction is performed [2]. This requires knowledge of the ventricle motion in 3D in the form of a dense motion vector field (MVF). Thus, the sparse motion field provided by the dynamic surface model has to be interpolated. In order to generate a dense MVF from scattered data several interpolation methods can be applied [26]. For computed tomography (CT) image reconstruction, different interpolation methods for cardiac motion were investigated by Forthmann et al. [27]. However, their main focus of the reconstruction was on imaging of the coronaries. Furthermore, C-arm projection data displays different contrast conditions and suffers from a lower temporal resolution than a conventional CT scanner. Therefore, it is not evident that the same interpolation methods yield the same results.

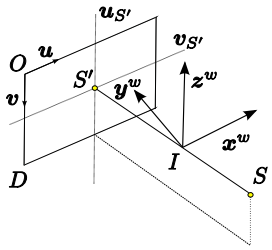

FIG. 1. Coordinate system of the C-arm system.

II. MATERIALS AND METHODS

A. Image Acquisition and C-arm CT Geometry

The basic C-arm CT geometry is illustrated in Figure 1. Parameter S denotes the X-ray source and S' is its perpendicular projection onto the detector plane D. The detector origin is denoted with O, and $\boldsymbol{u}$ and $\boldsymbol{v}$ are its row and column vector. Vectors $\boldsymbol{u}_{S'}$ and $\boldsymbol{v}_{S'}$ are the detector coordinates of the source projection S'. The origin of the 3D world-coordinate system $(\boldsymbol{x}^w, \boldsymbol{y}^w, \boldsymbol{z}^w)$ is set to the C-arm isocenter I, i.e. the center of rotation. The $\boldsymbol{z}^w$ axis is oriented along the rotation axis. The surface model control points as well as the motion vector field are given in world coordinates.

B. Surface Model

The proposed motion compensated reconstruction uses an MVF estimate given by a dynamic 3D surface model of the ventricle generated from the 2D projection data [3]. First, a standard FDK reconstruction is performed using all available 2D projections. This reconstruction still exhibits artifacts due to cardiac motion, but the reconstruction quality is sufficient for extraction of a static and preliminary 3D LV endocardium mesh using an algorithm proposed by Zheng et al. [28]. In the next step, the projections are assigned to a certain heart phase according to the acquired ECG signal. The static mesh is then projected onto the 2D projections belonging to a certain heart phase. The projected mesh silhouette is adjusted in the direction normal to each control point in order to match the ventricle border extracted by a learning based boundary detector [28]. The 2D deformation vector is then transformed into the 3D space and the 3D mesh is updated accordingly. As a result a 3D mesh is generated for every heart phase ϕ_k with its control points $\boldsymbol{p}_i(\phi_k) \in \mathbb{R}^3$, with $i = 1, \ldots, N$ where N is the number of control points [3]. For reconstruction a reference heart phase ϕ_0 is selected. The displacement or motion vectors point into the direction of the motion of the sparse control points between different heart phases. They are denoted as $\boldsymbol{d}_i(\phi_k) \in \mathbb{R}^3$ describing the distance of every control point between the reference heart phase ϕ_0 and the current heart phase ϕ_k. They can then be computed as follows

$$\boldsymbol{d}_i(\phi_k) = \boldsymbol{p}_i(\phi_k) - \boldsymbol{p}_i(\phi_0). \tag{1}$$

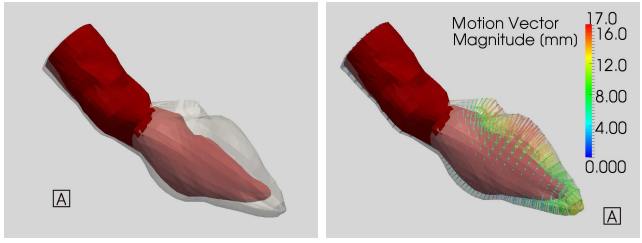

(a)Surface model for two different heart phases at end-diastole (transparent) and end-systole (solid).

(b)Sparse motion vectors $\boldsymbol{d}_i(\phi_k)$ between reference heart phase at end-diastole (transparent) and current phase at end-systole (solid).

FIG. 2. Illustration of the extracted surface model of the left ventricle.

An example of the left ventricle surface model for two different heart phases at end-diastole and end-systole is illustrated in Figure 2(a). In Figure 2(b) the sparse motion vectors $\boldsymbol{d}_i(\phi_k)$ are shown between reference heart phase and current heart phase.

C. Interpolation Methods

In order to perform a motion compensated tomographic reconstruction, a dense motion vector field (MVF) needs to be generated from the sparse MVF. Different interpolation methods were evaluated.

1. *Thin-Plate Splines (TPS)*

The deformation over time can be represented by a TPS transformation. The TPS approach assumes that the bending and stretching behavior of the left ventricle is similar to the bending of a thin plate. Thin-plate splines have already been applied to estimate cardiac vascular motion for CT data [29] and ventricular motion for MRI data [30]. Furthermore, they are widely used for elastic image registration of medical images [31, 32].
The TPS coordinate transformation with its displacements for an arbitrary point $\boldsymbol{x} \in \mathbb{R}^3$ is given as:

$$\boldsymbol{d}(\boldsymbol{x}, \phi_k) = \sum_{i=1}^{N} \boldsymbol{G}(\boldsymbol{x} - \boldsymbol{p}_i(\phi_k))\boldsymbol{c}_i(\phi_k) + \boldsymbol{A}(\phi_k)\boldsymbol{x} + \boldsymbol{b}(\phi_k), \tag{2}$$

where $\boldsymbol{c}_i(\phi_k) \in \mathbb{R}^3$ are the unknown spline coefficients of the TPS, $\boldsymbol{d}(\boldsymbol{x}, \phi_k)$ is the displacement vector at the point $\boldsymbol{x}$ and $\boldsymbol{p}_i(\phi_k) \in \mathbb{R}^3$ are the control points. The matrix $\boldsymbol{A}(\phi_k) \in \mathbb{R}^{3\times3}$ and the vector $\boldsymbol{b}(\phi_k) \in \mathbb{R}^3$ specify an additional affine transformation. The transformation's

kernel matrix $\boldsymbol{G}(\boldsymbol{x}) \in \mathbb{R}^{3\times3}$ of a point $\boldsymbol{x} \in \mathbb{R}^3$ for a 3D TPS is given according to [5]:

$$\boldsymbol{G}(\boldsymbol{x}) = r(\boldsymbol{x}) \cdot \boldsymbol{I}, \tag{3}$$

$$r(\boldsymbol{x}) = ||\boldsymbol{x}||_2 = \sqrt{x_1^2 + x_2^2 + x_3^2}, \tag{4}$$

where $\boldsymbol{I} \in \mathbb{R}^{3\times3}$ is the identity matrix. In order to solve Equation 2 for each ϕ_k, set $\boldsymbol{d}(\boldsymbol{x}, \phi_k) = \boldsymbol{d}_i(\phi_k)$ for $\boldsymbol{x} = \boldsymbol{p}_i(\phi_k)$. Farther away from the control points, the distance from the point to all control points is quite large, hence the first part of Equation 2 becomes a multiple of the average of $\boldsymbol{c}_i(\phi_k)$ and reduces to an affine transformation. Since Equation 2 is linear in $\boldsymbol{c}_i(\phi_k), \boldsymbol{A}(\phi_k)$, and $\boldsymbol{b}(\phi_k)$, it can be solved in a straightforward manner [5]. The resulting spline coefficients and affine parameters are inserted in Equation 2 in order to evaluate the spline at any arbitrary 3D point. A motion vector can therefore be computed for every voxel in the reconstructed volume.

2. *Linear Interpolation*

For linear interpolation, surface control points around the point $\boldsymbol{x}$ are determined and the resulting displacement vector $\boldsymbol{d}(\boldsymbol{x}, \phi_k)$ is a weighted sum of the corresponding displacement vectors:

$$\boldsymbol{d}(\boldsymbol{x}, \phi_k) = \sum_{i=1}^{N} \boldsymbol{G}^*(\boldsymbol{x} - \boldsymbol{p}_i(\phi_k))\boldsymbol{d}_i(\phi_k), \tag{5}$$

$$\boldsymbol{G}^*(\boldsymbol{x}) = f(\boldsymbol{x}) \cdot \boldsymbol{I}, \tag{6}$$

where f is a weighting function. Function f weights the displacement vectors according to the distance between the control point $\boldsymbol{p}_i(\phi_k)$ and the point $\boldsymbol{x}$. Three weighting functions are investigated.

a. Shepard's Method. Here an inverse distance weighting is applied according to the distance from the considered point to the n closest control points [6]. The function f is therefore defined as:

$$f(\boldsymbol{x}) = \frac{||\boldsymbol{x}||_2^{-1}}{\sum_{j=1}^{n} ||\boldsymbol{x}_j||_2^{-1}}, \tag{7}$$

with $\boldsymbol{x}_j = \boldsymbol{x} - \boldsymbol{p}_j(\phi_k)$. We empirically set n to 30 in this paper. Due to the density of the grid points, the number $n = 30$ corresponds to a range of approximately 2 cm around the grid point $\boldsymbol{x}$. Forthmann et al. evaluated $n = 1$ and $n = 128$ neighbors and stated that the number of points can be selected to be quite small, but one neighbor point may not be sufficient [27].

b. Smoothed Weighting Function. Here the function f is a cosine-based smoothing function:

$$f(\boldsymbol{x}) = \begin{cases} \frac{1}{N}(1 + \cos(\frac{||\boldsymbol{x}||_2 \cdot \pi}{R})) & ||\boldsymbol{x}||_2 \leq R \\ 0 & \text{otherwise,} \end{cases} \tag{8}$$

where $\mathcal{N}$ denotes a normalization constant so that $\sum_{j=1}^{N} f(\boldsymbol{x}_j) = 1$, and with $\boldsymbol{x}_j = \boldsymbol{x} - \boldsymbol{p}_j(\phi_k)$. The radius

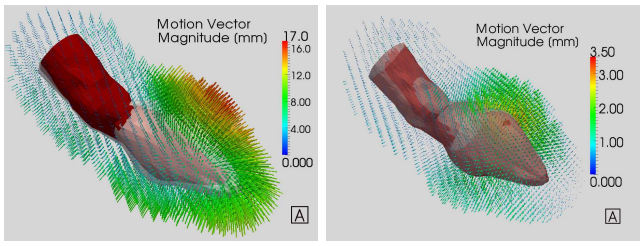

(a)Between reference heart phase at end-diastole and current phase at end-systole.

(b)Between reference heart phase close to end-diastole and current phase at end-diastole.

FIG. 3. Illustration of a dense MVF of the human data set computed with TPS. The number of vectors displayed has been reduced in order to permit visualization of MVF characteristics.

R is empirically set to 2 cm. We picked 2 cm because it seemed reasonable and included ≈ 30 points, but dependence on the region of interest size has not been investigated and is beyond the scope of this paper.

c. Simple Averaging. Here the resulting displacement vector $\boldsymbol{d}(\boldsymbol{x}, \phi_k)$ is a simple average of the displacement vectors at the surrounding control points. Thus the function f, with M denoting the number of control points located within a sphere of radius R around $\boldsymbol{x}$ is defined as:

$$f(\boldsymbol{x}) = \begin{cases} \frac{1}{M} & ||\boldsymbol{x}||_2 \leq R \\ 0 & \text{else.} \end{cases} \tag{9}$$

In this study an empiric radius $R = 2$ cm is used. We picked the same radius as in Paragraph II C 2 b.

D. Cutting

In order to reduce the computational complexity we assume that the left ventricle is the central moving organ inside the scan field of view. This assumption is justified due to the acquisition protocol where for the most part only the left heart ventricle is filled with contrast during the procedure. Therefore, a dense MVF is estimated in the neighborhood of the ventricle. The considered set of points $\mathcal{P}$ for which a motion vector is estimated is given as:

$$\mathcal{P} = \{\boldsymbol{x} \mid ||\boldsymbol{x} - \boldsymbol{p}_{\boldsymbol{x}}(\phi_k)||_2 \leq l\}, \tag{10}$$

where $\boldsymbol{p}_{\boldsymbol{x}}(\phi_k)$ is the closest surface control point to the current point $\boldsymbol{x}$. The distance l was heuristically set to 2 cm around the surface model in the heart phase ϕ_0. In Figure 3(a), an MVF of the human data set h_1 between the reference heart phase at end-diastole and the current heart phase at end-systole is illustrated for the TPS. The MVF of h_1 between the reference heart phase close to end-diastole and the current heart phase at end-diastole is illustrated for the TPS in Figure 3(b).

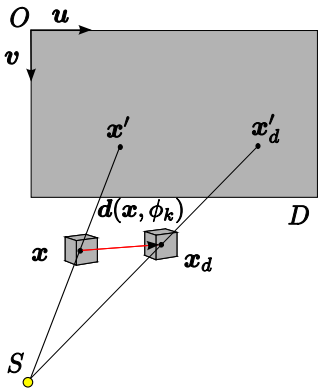

FIG. 4. A simplified scheme of the voxel-based motion compensation.

E. Motion Compensation

The motion compensated reconstruction algorithm used here is based on the FDK formulation. The estimated motion vector field is incorporated into a voxel-driven filtered backprojection reconstruction algorithm. The motion correction is applied during the backprojection step by shifting the voxel to be reconstructed according to the motion vector field. In Figure 4, a schematic illustration of the motion compensated backprojection is given. Parameter S denotes the X-ray source, D the detector plane and O the origin of the image plane. The motion vector $\boldsymbol{d}(\boldsymbol{x}, \phi_k)$ at voxel position $\boldsymbol{x}$ given in world coordinates indicates a 3D motion to the point $\boldsymbol{x}_d$. $\boldsymbol{x}'$ and $\boldsymbol{x}'_d$ are the perspective projections of $\boldsymbol{x}$ and $\boldsymbol{x}_d$ with viewpoint S. Instead of accumulating the 2D projection value at position $\boldsymbol{x}'$ to the position $\boldsymbol{x}$, the value at $\boldsymbol{x}'_d$ is backprojected. A more detailed explanation of the algorithm can be found in Schäfer et al. [2].

III. EXPERIMENTAL SETUP

A. Phantom Data

The algorithm presented here has been applied to a ventricle data set comparable to the XCAT phantom [33, 34]. The bloodpool density of the left ventricle was set to $2.5\,\mathrm{g/cm^3}$, the density of the myocardium wall to $1.5\,\mathrm{g/cm^3}$ and the blood in the aorta to $2.0\,\mathrm{g/cm^3}$. It is assumed that all materials have the same absorption as water. We simulated data using a clinical protocol with the following parameters: 395 projection images simulated equi-angularly over an angular range of 200° at a frame rate of 60 fps with a size of 620×480 pixels at an isotropic resolution of 0.62 mm/pixel. The distance from source to detector was 120 cm and from source to isocenter 78 cm, leading to a resolution of about 0.4 mm in the isocenter. The surface model consisted of 40 heart phases between subsequent R-peaks and 957 control points uniformly distributed over the left ventricle. The image reconstruction was performed on an image volume of $(25.6\,\mathrm{cm})^3$ distributed on a 256^3 voxel grid. Electrophysiological parameters extracted from the surface model are given in Table I.

B. Porcine Data

The porcine data set was acquired on an Axiom Artis dTA C-arm system (Siemens AG, Healthcare Sector, Forchheim, Germany). We acquired data using the same clinical protocol as described in Section III A. The contrast agent was administered by a pigtail catheter directly into the left heart ventricle. The surface model consisted of 30 heart phases between subsequent R-peaks and 961 control points equally distributed over the left ventricle. Due to memory restrictions, image reconstruction was performed on an image volume of $(21.8\,\mathrm{cm})^3$ distributed on a 256^3 voxel grid with a resolution of 0.85 mm. Electrophysiological parameters extracted from the surface model are given in Table I.

C. Clinical Human Data

The first data set h_1 was acquired on an Artis zee C-arm system (Siemens AG, Healthcare Sector, Forchheim, Germany). It consists of 133 projection images acquired over an angular range of 200° in 5 s with a size of 960×960 pixels at an isotropic resolution of 0.18 mm/pixel (about 0.12 mm in isocenter) at a frame rate of 30 fps. The distance from source to detector was 120 cm and from source to isocenter 78 cm. The contrast agent was administered by a pigtail catheter directly into the left heart ventricle. The surface model consisted of 26 heart phases between subsequent R-peaks and 961 control points equally distributed over the first section of the left ventricle. Image reconstruction was performed on an image volume of $(14.1\,\mathrm{cm})^3$ distributed on a 256^3 voxel grid. The data sets h_2 and h_3 were acquired on an Artis zeego C-arm system (Siemens AG, Healthcare Sector, Forchheim, Germany). They consist of 133 projection images acquired over an angular range of 200° in 5 s with a size of 960×960 pixels at an isotropic resolution of 0.31 mm/pixel (about 0.2 mm in isocenter). The frame rate, source-detector and source-isocenter distances were the same as for h_1. The left heart ventricle was again filled with contrast directly by a pigtail catheter. The surface model consisted of 25 and 30 heart phases between subsequent R-peaks for h_2 and h_3 respectively and 906 control points equally distributed over the left ventricle. Image reconstruction was performed on an image volume of $(19.2\,\mathrm{cm})^3$ distributed on a 256^3 voxel grid. Electrophysiological parameters for h_1, h_2 and h_3 extracted from the surface model are given in Table I.

TABLE I. Electrophysiological data parameters extracted from the surface model: ejection fraction (EF), stroke volume (SV), end-diastolic volume (EDV), end-systolic volume (ESV).

	heart rate [bpm]	EF [%]	SV [ml]	EDV [ml]	ESV [ml]
Phantom	≈75	30	42.03	135.82	93.79
Porcine	≈103.3±24.2	46	40.05	87.44	47.40
Human h_1	≈61.6±1.7	75	50.43	67.50	17.07
Human h_2	≈62.9±2.9	59	74.63	125.88	51.24
Human h_3	≈55.3±9.3	63	103.03	167.38	61.56

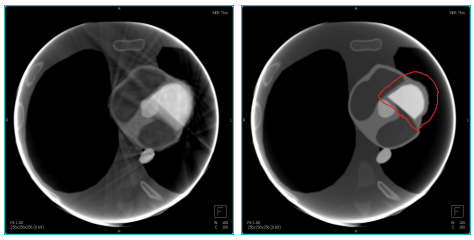

(a)Standard FDK reconstruction of the dynamic phantom.

(b)Gold standard FDK reconstruction of the static heart phantom of heart phase 40% and ROI (red contour) used for evaluation.

FIG. 5. Transverse slice of a reconstructed image of the dynamic FDK reconstruction result and the gold standard reconstruction of the phantom left ventricle. The ROI used for image quality metric measurements is shown as the red contour.

D. Quantitative Evaluation

1. Phantom Image Quality in 3D Image Space

For the dynamic phantom data set the 3D error and a quantitative 3D image metric can be evaluated. In order to measure only the artifacts introduced by the heart motion, the FDK reconstruction of the static heart phantom of the same heart phase is used as gold standard. Heart phases from 10% to 100% with 10% increment were evaluated. The reconstruction of the static phantom is done with the same geometric reconstruction parameters as the motion compensated reconstructions and the standard FDK reconstruction of the dynamic phantom (see Figure 5(a)). The ground truth of the phantom is not used due to the fact that only the artifacts coming from the heart motion should be measured and evaluated by using FDK as a gold standard. Other cone-beam or truncation artifacts are identical in the images and can be neglected. Let $\boldsymbol{y} = \{y_i \,|\, i = 1, 2, \ldots, N\}$ be the gold standard image and $\boldsymbol{x} = \{x_i \,|, i = 1, 2, \ldots, N\}$ the motion compensated or standard FDK reconstructed image. The error as well as image quality metric were evaluated in a region of interest (ROI) around the ventricle. An example of the ROI is illustrated in Figure 5(b).

a. Normalized Root Mean Square Error (nRMSE). The nRMSE was used to quantify the 3D reconstruction error of the motion compensated reconstructions or standard FDK reconstructions compared to the gold standard FDK of the static phantom. The nRMSE can be computed as follows

$$\text{nRMSE} = \frac{1}{\max(\boldsymbol{y}) - \min(\boldsymbol{y})} \sqrt{\frac{1}{N} \sum_{i=1}^{N} (x_i - y_i)^2}, \quad (11)$$

where N denotes the number of voxels inside the region of interest (ROI). All results were averaged over the heart phases, resulting in the overall nRMSE.

b. Universal Quality Index (UQI). The 3D image quality was evaluated with the universal image quality index (UQI) [35]. The UQI ranges from -1 to 1, where 1 is the best value achieved when $y_i = x_i$ for all $i = 1, 2, \ldots, N$. The UQI is defined as

$$UQI = \frac{4 \cdot \sigma_{xy} \cdot \overline{x} \cdot \overline{y}}{\left(\sigma_x^2 + \sigma_y^2\right) \left[(\overline{x})^2 + (\overline{y})^2\right]}, \quad (12)$$

where $\overline{x}, \overline{y}$ represent the mean values, σ_x^2, σ_y^2 the variances, and σ_{xy} the cross correlation inside the ROI. All results were averaged over the heart phases, resulting in the overall UQI.

2. Dice Similarity (DSC) Coefficient in 2D Projection Space

In order to compare the reconstruction quality of the motion compensated reconstruction algorithm, maximum intensity forward projections (MIPs) of the compensated LVs were generated. Binary mask images $\mathcal{B}_{FW}(\phi_k)$ were created from the MIPs by thresholding where only the left ventricle is visible. A value equal to zero defines background and a non-zero value defines the ventricle shape. These binary images were compared to the segmented 2D projections from which the original surface model and the MVF were built, denoted as $\mathcal{B}_{GS}(\phi_k)$. The overlap of the binarized image and the segmented 2D projections was analyzed with the Dice similarity coefficient (DSC) [36]. The DSC is defined in the range of $[0, 1]$, where 0 means no overlap and 1 defines a perfect match between the two compared images. All results were averaged over the heart phases, resulting in the overall Dice coefficient. The DSC is defined as

$$DSC = \frac{2|\mathcal{B}_{FW}(\phi_k) \cap \mathcal{B}_{GS}(\phi_k)|}{|\mathcal{B}_{FW}(\phi_k)| + |\mathcal{B}_{GS}(\phi_k)|} \quad (13)$$

3. Mean Contour Deviation ϵ in 2D Projection Space

Since the motion compensated reconstruction mainly improves the accuracy of the ventricle contour, the similarity of the contours was evaluated. The contour

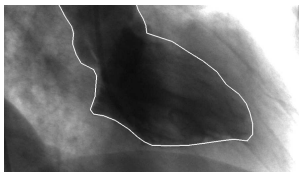

(a)Gold standard segmentation of the ventricle bloodpool in 2D.

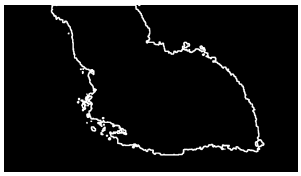

(b)Extracted contour $\mathcal{C}_{FW}(\phi_k)$ of the MIP projection image.

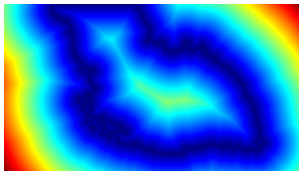

(c)Euclidean distance transformed image $\Phi(\mathcal{C}_{FW}(\phi_k))$. Dark color represents smaller distance and lighter color a larger contour distance.

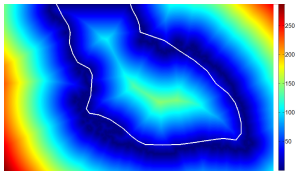

(d)Euclidean distance transformed image $\Phi(\mathcal{C}_{FW}(\phi_k))$ overlaid with the contour $\mathcal{C}_{GS}(\phi_k)$. For the computation of $\epsilon(\phi_k)$ only the underlying values of $\Phi(\mathcal{C}_{FW}(\phi_k))$ are used.

FIG. 6. Different contour projection images for quantitative evaluation.

$\mathcal{C}_{FW}(\phi_k)$ and $\mathcal{C}_{GS}(\phi_k)$ of the binary masks of the forward projection $\mathcal{B}_{FW}(\phi_k)$ and the gold standard projection $\mathcal{B}_{GS}(\phi_k)$ were extracted. The contour $\mathcal{C}_{FW}(\phi_k)$ is extracted by morphological operations from $\mathcal{B}_{FW}(\phi_k)$. The contour $\mathcal{C}_{GS}(\phi_k)$ is given by the dynamic 3D surface model generation (see Section II B). In Figure 6(a) the boundary $\mathcal{C}_{GS}(\phi_k)$ of the left ventricle is illustrated which is used as gold standard. Figure 6(b) shows $\mathcal{C}_{FW}(\phi_k)$. A distance transform $\Phi(\mathcal{C}_{FW}(\phi_k))$ of the binary contour images $\mathcal{C}_{FW}(\phi_k)$ is defined by computing the Euclidean distance of every pixel to the contour $\mathcal{C}_{FW}(\phi_k)$. An example of a distance transformed image $\Phi(\mathcal{C}_{FW}(\phi_k))$ is shown in Figure 6(c). An overlay of $\mathcal{C}_{GS}(\phi_k)$ and $\Phi(\mathcal{C}_{FW}(\phi_k))$ is shown in Figure 6(d). The distance transformed image is sampled only at the indices where $\mathcal{C}_{GS}(\phi_k)$ is non-zero:

$$\epsilon(\phi_k) = \frac{1}{N_c} \sum_{n=1}^{N_c} \Phi(\mathcal{C}_{FW}(\phi_k))_n, \qquad (14)$$

where N_c denotes the number of pixels where $\mathcal{C}_{GS}(\phi_k)$ is non-zero. All results were averaged over the heart phases, resulting in the overall mean contour deviation ϵ. A small ϵ denotes similar contours over all heart phases.

IV. RESULTS AND DISCUSSION

A. Phantom Data

The quantitative 3D results of the dynamic phantom model are presented in Table II. The smallest nRMSE is attained by the TPS and Shepard's method,

TABLE II. The nRMSE and the UQI of the dynamic phantom model. Expressed as mean value ± standard deviation. The best values are marked in bold.

	Phantom	
	nRMSE	UQI [%]
TPS	$\mathbf{0.047 \pm 0.004}$	98.5 ± 0.3
Shepard	$\mathbf{0.047 \pm 0.004}$	$\mathbf{98.9 \pm 0.2}$
Smoothed Weighting Fct.	0.048 ± 0.004	98.8 ± 0.2
Simple Averaging	0.050 ± 0.006	98.7 ± 0.2
Standard FDK	0.080 ± 0.019	96.22 ± 1.6

TABLE III. Dice coefficient and mean contour deviation ϵ for the left ventricle of the phantom data set. Expressed as mean value ± standard deviation. The best values are marked in bold.

	Phantom		
	Dice [pixel]	ϵ [pixel]	ϵ [mm]
TPS	$\mathbf{0.96 \pm 0.02}$	$\mathbf{2.75 \pm 0.43}$	$\mathbf{1.71 \pm 0.27}$
Shepard	0.95 ± 0.02	3.33 ± 0.31	2.06 ± 0.20
Smoothed Weighting Fct.	0.95 ± 0.02	3.33 ± 0.27	2.06 ± 0.17
Simple Averaging	0.94 ± 0.02	3.64 ± 0.33	2.26 ± 0.20
Standard FDK	0.94 ± 0.03	4.66 ± 1.91	2.89 ± 1.18

the smoothed weighting function has a slightly larger error. The UQI for all motion compensated reconstructions results in values around 99%. In Table III the Dice and the contour deviation ϵ in 2D projection space for the phantom left ventricle are reported. The TPS approach, Shepard's method and the smoothed weighting function show equivalently good results. The contour deviation (ϵ) of the TPS improved by about 1.91 pixels which corresponds to 1.18 mm compared to the standard FDK. The standard deviation is also much smaller with the TPS compared to the standard reconstruction. The Dice coefficient is not very sensitive and shows similar results between all interpolation methods as well as for the FDK reconstruction. In Figure 7 the results of the motion compensated reconstructions of the phantom left ventricle using different interpolation methods are illustrated. There are minor visible differences in the endocardium

TABLE IV. Dice coefficient and mean contour deviation ϵ for the left ventricle of the porcine data set. Expressed as mean value ± standard deviation.

	Porcine		
	Dice [pixel]	ϵ [pixel]	ϵ [mm]
TPS	$\mathbf{0.92 \pm 0.01}$	$\mathbf{3.67 \pm 0.18}$	$\mathbf{2.28 \pm 0.11}$
Shepard	$\mathbf{0.92 \pm 0.01}$	3.88 ± 0.19	2.39 ± 0.12
Smoothed Weighting Fct.	$\mathbf{0.92 \pm 0.01}$	4.50 ± 0.39	2.77 ± 0.24
Simple Averaging	$\mathbf{0.92 \pm 0.01}$	4.05 ± 0.20	2.51 ± 0.12
Standard FDK	0.90 ± 0.02	4.64 ± 0.49	2.88 ± 0.30

TABLE V. Dice coefficient and mean contour deviation ϵ for the left ventricle of the human data sets. Expressed as mean value ± standard deviation.

	Human h_1		
	Dice [pixel]	ϵ [pixel]	ϵ [mm]
TPS	$\mathbf{0.93 \pm 0.01}$	$\mathbf{9.15 \pm 1.22}$	$\mathbf{1.65 \pm 0.22}$
Shepard	0.91 ± 0.02	10.29 ± 2.07	1.85 ± 0.33
Smoothed Weighting Fct.	0.91 ± 0.02	10.92 ± 3.02	1.97 ± 0.54
Simple Averaging	0.91 ± 0.03	11.74 ± 2.81	2.11 ± 0.51
Standard FDK	0.88 ± 0.03	17.60 ± 10.0	3.17 ± 1.80
	Human h_2		
	Dice [pixel]	ϵ [pixel]	ϵ [mm]
TPS	$\mathbf{0.93 \pm 0.01}$	$\mathbf{6.70 \pm 0.74}$	$\mathbf{2.08 \pm 0.23}$
Shepard	$\mathbf{0.93 \pm 0.02}$	6.99 ± 1.37	2.17 ± 0.42
Smoothed Weighting Fct.	$\mathbf{0.93 \pm 0.02}$	7.17 ± 1.43	2.22 ± 0.44
Simple Averaging	$\mathbf{0.93 \pm 0.02}$	7.40 ± 1.98	2.29 ± 0.61
Standard FDK	0.89 ± 0.06	11.02 ± 5.80	3.42 ± 1.80
	Human h_3		
	Dice [pixel]	ϵ [pixel]	ϵ [mm]
TPS	$\mathbf{0.88 \pm 0.02}$	$\mathbf{8.64 \pm 0.98}$	$\mathbf{2.68 \pm 0.30}$
Shepard	0.85 ± 0.03	12.13 ± 1.93	3.76 ± 0.60
Smoothed Weighting Fct.	0.85 ± 0.03	12.10 ± 1.88	3.75 ± 0.58
Simple Averaging	0.85 ± 0.03	12.38 ± 2.05	3.84 ± 1.19
Standard FDK	0.83 ± 0.06	13.64 ± 5.81	4.23 ± 1.80

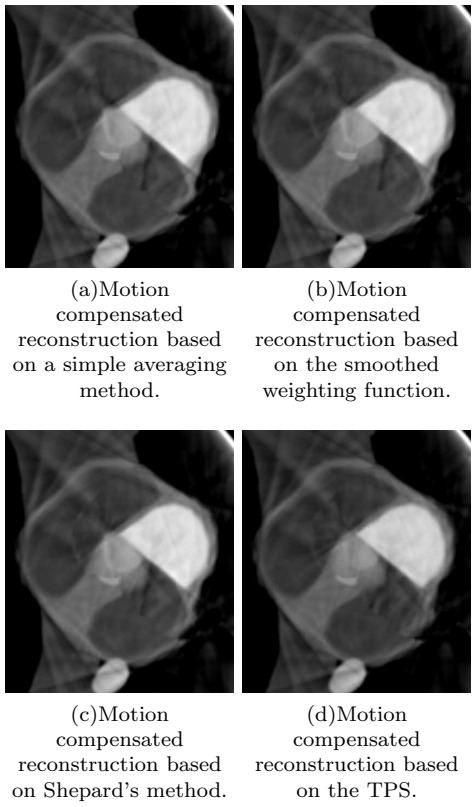

(a)Motion compensated reconstruction based on a simple averaging method.

(b)Motion compensated reconstruction based on the smoothed weighting function.

(c)Motion compensated reconstruction based on Shepard's method.

(d)Motion compensated reconstruction based on the TPS.

FIG. 7. Detail of an axial slice of the reconstruction images of the phantom left ventricle of a heart phase of 40% using the different interpolation methods.

border. All interpolation methods show deformation artifacts outside the region of interest.

B. Porcine Data

In Table IV the results for the porcine left ventricle are reported. It can be seen that the best motion compensated reconstruction can be achieved with the TPS interpolation method compared to a standard reconstruction. The mean contour deviation (ϵ) improved by about 0.97 pixels which corresponds to 0.60 mm compared to the standard FDK reconstructions. The improvement is relatively small due to the fact that the pig had a poor ejection fraction of about 46%. In Figure 8 the results of different reconstructions of the porcine left ventricle are illustrated. The standard reconstruction in Figure 8(a) exhibits blurring around the LV. In Figure 8(b) it can be observed that the ECG-gated reconstruction lacks LV structure and suffers from artifacts from the pigtail catheter. In comparison, the motion compensated reconstruction shows an expansion in diastole and contraction in systole of the LV, respectively (Fig.8(c),8(d)).

C. Clinical Data

In Table V the results for the human left ventricles are listed. The best motion compensated reconstructions are clearly performed with the TPS for all three cases. The respective contour deviation (ϵ) improved by about 8.45 pixels which corresponds to 1.52 mm, about 4.32 pixels which corresponds to 1.34 mm and about 5 pixels which corresponds to 1.55 mm compared to the standard FDK. The standard deviation is also much smaller with the TPS compared to the standard reconstructions. The widely used Shepard's method and the smoothed weighting function provides slightly inferior results compared to the TPS. The papillary muscle boundary is sharper in the TPS interpolated volumes. The Dice coefficient shows similar results between all interpolation methods as well as for the FDK reconstruction, thus is less sensitive compared to the contour deviation. The standard reconstruction in Figure 9(a) exhibits blurring around the LV. In Figure 9(b) it can be observed that the ECG-gated reconstruction lacks LV structure and suffers from artifacts. In comparison, the motion compensated reconstruction shows an expansion in diastole and contraction in systole of the LV, respectively (Fig.9(c),9(d)). In Figure 10 the results of different reconstructions of the human left ventricle h_1 are

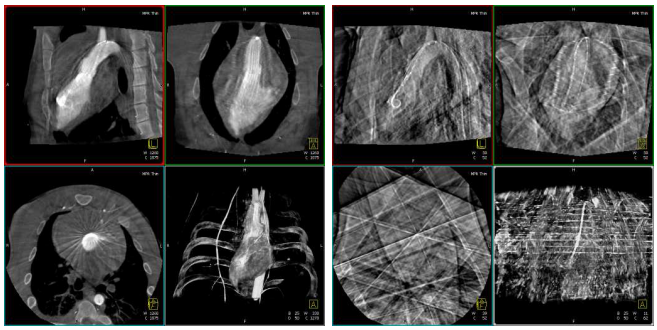

(a)Standard FDK reconstruction.

(b)Nearest-Neighbor ECG-gated reconstruction for end-systolic heart phase (5 views).

(c)Motion compensated reconstruction for end-systolic heart phase (relative heart phase of 30%).

(d)Motion compensated reconstruction for end-diastolic heart phase (relative heart phase of 95%).

FIG. 8. Multi-planar reconstruction images (long axis view top left and right, short axis view bottom left) and volume rendering (bottom right) of the reconstruction results of the porcine left ventricle with the TPS interpolation (W 1260 HU, C 1075 HU, slice thickness 0.85 mm). The ECG-gated reconstruction was windowed to be visually comparable.

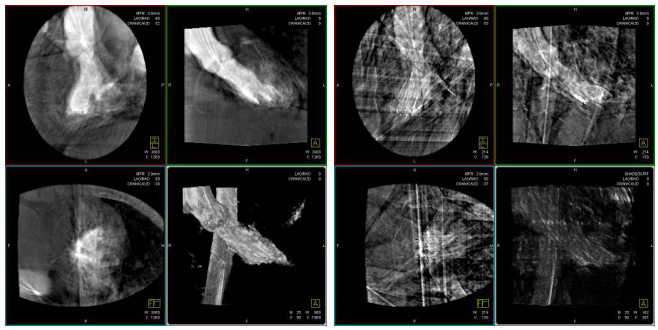

(a)Standard FDK reconstruction.

(b)Nearest-Neighbor ECG-gated reconstruction for end-systolic heart phase (5 views).

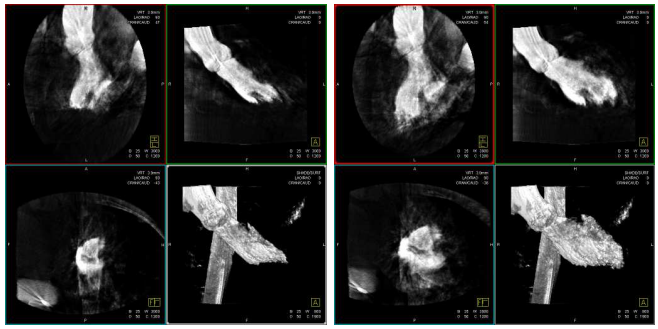

(c)Motion compensated reconstruction for end-systolic heart phase (relative heart phase of 20%).

(d)Motion compensated reconstruction for end-diastolic heart phase (relative heart phase of 70%).

FIG. 9. Multi-planar reconstruction images (long axis view top left and right, short axis view bottom left) and volume rendering (bottom right) of the reconstruction results of the human left ventricle h_1 with the TPS interpolation (W 3000 HU, C 1200 HU, slice thickness 3.0 mm). The ECG-gated reconstruction was windowed to be visually comparable.

illustrated. The motion compensated reconstructions all show an expansion of the left ventricle, but slightly different shapes.

D. Limitations

The interpolation result and hence the motion compensated reconstruction is dependent on the robustness and stability of the extracted surface model. The method is robust with respect to higher heart rates up to 100 bpm or even more. The porcine model had a heart rate of ≈ 100 bpm. However, if the heart beat is quite arrhythmic, the assignment of the projection images to a certain heart phase becomes ambiguous and thus the generation of the dynamic surface model is not unique. This influence and impact on the clinical application needs to be evaluated in the near future.

V. CONCLUSIONS

In this paper, we investigated the influence of different motion interpolation methods. The interpolation is used to compute a dense motion vector field from a sparse one for the purpose of motion compensation in left ventricle tomographic reconstruction. The sparse motion vector fields were generated by a dynamic surface model and interpolated by a thin-plate spline, Shepard's method, a smoothed weighting based approach and simple averaging. The best quantitative results (Dice coefficient, mean contour deviation) for a phantom, a porcine and three human data sets were achieved using the TPS interpolation approach. Shepard's method and the smoothed weighting function might be a good compromise between computational efficiency and accuracy. In conclusion, motion compensated reconstruction improved the reconstruction results compared to a standard reconstruction. As a next step, the integration into the clinical workflow needs to be evaluated. In general, the framework of motion estimation using a surface model and motion interpolation

(a)Motion compensated reconstruction with simple averaging interpolation method.

(b)Motion compensated reconstruction with smoothed weighting function interpolation method.

(c)Motion compensated reconstruction with Shepard's interpolation method.

(d)Motion compensated reconstruction with TPS interpolation method.

FIG. 10. Coronal slice of the reconstruction images (long axis view) of the motion compensated reconstruction results of the human left ventricle h_1 and an end-diastolic heart phase of 70% (W 3000 HU, C 1200 HU, slice thickness 3.0 mm).

to a dense MVF provides the ability for tomographic reconstruction using a motion compensation technique.

ACKNOWLEDGEMENT

The authors gratefully acknowledge funding support from the NIH grant R01 HL087917 and of the Erlangen Graduate School in Advanced Optical Technologies (SAOT) by the German Research Foundation (DFG) in the framework of the German excellence initiative.

Disclaimer: The concepts and information presented in this paper are based on research and are not commercially available.

[1] Feldkamp, L., Davis, L., Kress, J.: Practical cone-beam algorithm. Journal of the Optical Society of America A **1**(6) (June 1984) 612–619

[2] Schäfer, D., Borgert, J., Rasche, V., Grass, M.: Motion-compensated and gated cone beam filtered back-projection for 3-D rotational X-Ray angiography. IEEE Transactions on Medical Imaging **25**(7) (July 2006) 898–906

[3] Chen, M., Zheng, Y., Müller, K., Rohkohl, C., Lauritsch, G., Boese, J., Funka-Lea, G., Hornegger, J., Comaniciu, D.: Automatic extraction of 3D dynamic left ventricle model from 2D rotational angiocardiogram. In Fichtinger, G., Martel, A., Peters, T., eds.: Proceedings of the Medical Imaging Conference and Computer Assisted Intervention (MICCAI) 2011. Volume 6893 of Lecture Notes in Computer Science. (September 2011) 471–478

[4] Bookstein, F.L.: Principal warps: Thin-plate splines and the decomposition of deformations. IEEE Transactions on Pattern Recognition and Machine Intelligence **11**(6) (June 1989) 567–585

[5] Davis, M.H., Khotanzad, A., Flamig, D.P., Harms, S.E.: A physics-based coordinate transformation for 3-D image matching. IEEE Transactions on Medical Imaging **16**(3) (June 1997) 317–328

[6] Shepard, D.: A two-dimensional interpolation function for irregularly-spaced data. In: Proceedings of the 1968 23rd ACM National Conference. (1968) 517–524

[7] Sheehan, F.H., Bolson, E.L.: Defining normal left ventricular wall motion from contrast ventriculograms. Physiological Measurement **24**(3) (August 2003) 785–792

[8] Medina, R., Garreau, M., Lebreton, H., Jugo, D.: Three-dimensional reconstruction of the left ventricle from two angiographic views. In: Proceedings of the IEEE Engineering in Medicine and Biology Society (EMBS). Volume 2. (October 1997) 569–572

[9] Medina, R., Garreau, M., Toro, J., Breton, H.L., Coatrieux, J.L., Jugo, D.: Markov random field modeling for three-dimensional reconstruction of the left ventricle in cardiac angiography. IEEE Transactions on Medical Imaging **25**(8) (August 2006) 1087–1100

[10] Sato, Y., Moriyama, M., Hanayama, M., Naito, H., Tamura, S.: Acquiring 3D models of non-rigid moving objects from time and viewpoint varying image sequences: A step toward left ventricle recovery. IEEE Transactions on Pattern Analysis and Machine Intelli-

gence **19**(3) (March 1997) 253–258

[11] Moriyama, M., Sato, Y., Naito, H., Hanayama, M., Ueguchi, T., Harada, T., Yoshimoto, F., Tamura, S.: Reconstruction of time-varying 3-D left-ventricular shape from multiview X-ray cineangiocardiograms. IEEE Transactions on Medical Imaging **21**(7) (July 2002) 773–785

[12] Desjardins, B., Kazerooni, E.A.: ECG-gated cardiac CT. American Journal of Roentgenology **182**(4) (April 2004) 993–1010

[13] Blondel, C., Malandain, G., Vaillant, R., Ayache, N.: Reconstruction of coronary arteries from a single rotational X-Ray projection sequence. IEEE Transactions on Medical Imaging **25**(5) (May 2006) 653–663

[14] Hansis, E., Schäfer, D., Dössel, O., Grass, M.: Projection-based motion compensation for gated coronary artery reconstruction from rotational X-ray angiograms. Physics in Medicine and Biology **53**(14) (July 2008) 3807–3820

[15] Rohkohl, C., Lauritsch, G., Biller, L., Prümmer, M., Boese, J., Hornegger, J.: Interventional 4D motion estimation and reconstruction of cardiac vasculature without motion periodicity assumption. Medical Image Analysis **14**(5) (October 2010) 687–694

[16] Schwemmer, C., Rohkohl, C., Lauritsch, G., Müller, K., Hornegger, J.: Residual motion compensation in ECG-gated cardiac vasculature reconstruction. In Noo, F., ed.: Proceedings of the Second International Conference on Image Formation in X-ray Computed Tomography. (June 2012) 259–262

[17] Lauritsch, G., Boese, J., Wigström, L., Kemeth, H., Fahrig, R.: Towards cardiac C-arm computed tomography. IEEE Transactions on Medical Imaging **25**(7) (July 2006) 922–934

[18] Prümmer, M., Hornegger, J., Lauritsch, G., Wigström, L. Girard-Hughes, E., Fahrig, R.: Cardiac C-arm CT: A unified framework for motion estimation and dynamic CT. IEEE Transactions on Medical Imaging **28**(11) (November 2009) 1836–1849

[19] Donoho, D.L.: Compressed sensing. IEEE Transactions on Information Theory **54**(4) (April 2006) 1249–1306

[20] Sidky, E.Y., Pan, X.: Image reconstruction in circular cone-beam computed tomography by constrained, total-variation minimization. Physics in Medicine and Biology **53**(17) (August 2008) 4777–4807

[21] Chen, G.H., Tang, J., Leng, S.: Prior image constrained compressed sensing (PICCS): A method to accurately reconstruct dynamic CT images from highly undersampled projection data sets. Medical Physics **35**(2) (February 2008) 660–663

[22] Chen, G.H., Tang, J., Hsieh, J.: Temporal resolution improvement using PICCS in MDCT cardiac imaging. Medical Physics **36**(6) (June 2009) 2130–2135

[23] Theriault-Lauzier, P., Tang, J., Chen, G.H.: Prior image constrained compressed sensing: Implementation and performance evaluation. Medical Physics **39**(1) (January 2012) 66–80

[24] Chen, G.H., Theriault-Lauzier, P., Tang, J., Nett, B., Leng, S., Zambelli, J., Zhihua, Q., Bevins, N., Raval, A., Reeder, S., Rowley, H.: Time-resolved interventional cardiac C-arm cone-beam CT: An application of the PICCS algorithm. IEEE Transactions on Medical Imaging **31**(4) (April 2012) 907–923

[25] Theriault-Lauzier, P., Tang, J., Chen, G.H.: Time-resolved cardiac interventional cone-beam CT reconstruction from fully truncated projections using the prior image constrained compressed sensing (PICCS) algorithm. Physics in Medicine and Biology **57**(9) (May 2012) 2461–2476

[26] Amidror, I.: Scattered data interpolation methods for electronic imaging systems: A survey. Journal of Electronic Imaging **11**(2) (April 2002) 157–176

[27] Forthmann, P., van Stevendaal, U., Grass, M., Köhler, T.: Vector field interpolation for cardiac motion compensated reconstruction. In: Proceedings of the IEEE Nuclear Science Symposium and Medical Imaging Conference (NSS/MIC). (October 2008) 4157–4160

[28] Zheng, Y., Barbu, A., Georgescu, B., Scheuering, M., Comaniciu, D.: Four-chamber heart modeling and automatic segmentation for 3D cardiac CT volumes using marginal space learning and steerable features. IEEE Transactions on Medical Imaging **27**(11) (November 2008) 1668–1681

[29] Isola, A.A., Metz, C.T., Schaap, M., Klein, S., Niessen, W.J., Grass, M.: Coronary segmentation based motion corrected cardiac CT reconstruction. In: Proceedings of the IEEE Nuclear Science Symposium and Medical Imaging Conference (NSS/MIC). (October 2010) 2026–2029

[30] Suter, D., Chen, F.: Left ventricular motion reconstruction based on elastic vector splines. IEEE Transactions on Medical Imaging **19**(4) (April 2000) 295–305

[31] Rohr, K., Stiehl, H.S., Sprengel, R., Buzug, T.M., Weese, J., Kuhn, M.H.: Landmark-based elastic registration using approximating thin-plate splines. IEEE Transactions on Medical Imaging **20**(6) (June 2001) 526–534

[32] Sprengel, R., Rohr, K., Stiehl, H.S.: Thin-plate spline approximation for image registration. In: Proceedings of the 18th Annual International Conference of the IEEE Engineering in Medicine and Biology Society (EMBS). Volume 5. (November 1996) 1190–1191

[33] Maier, A., Hofmann, H.G., Schwemmer, C., Hornegger, J., Keil, A., Fahrig, R.: Fast simulation of X-ray projections of spline-based surfaces using an append buffer. Physics in Medicine and Biology **57**(19) (October 2012) 6193–6210

[34] Segars, W.P., Mahesh, M., Beck, T.J., Frey, E.C., Tsui, B.M.W.: Realistic CT simulation using the 4D XCAT phantom. Medical Physics **35**(8) (August 2008) 3800–3808

[35] Wang, Z., Bovik, A.C.: A universal image quality index. IEEE Signal Processing Letters **9**(3) (March 2002) 81–84

[36] Zou, K.H., Warfield, S.K., Bharatha, A., Tempany, C.M.C., Kaus, M.R., Haker, S.J., Wells, W.M.W., Jolesz, F.A., Kikinis, R.: Statistical validation of image segmentation quality based on a spatial overlap index: Scientific reports. Academic Radiology **11**(2) (2004) 178–189